5-2-2006

Unconventional optical imaging using a high speed, neural network based smart sensor

William W. Arrasmith

Unconventional optical imaging using a high speed, neural network based smart sensor

William W. Arrasmith

Florida Institute of Technology, 150 W. University Blvd, Melbourne, FL 32901

ABSTRACT

The advancement of neural network methods and technologies is finding applications in many fields and disciplines of interest to the defense, intelligence, and homeland security communities. Rapidly re-configurable sensors for real or near-real time signal or image processing can be used for multi-functional purposes such as image compression, target tracking, image fusion, edge detection, thresholding, pattern recognition, and atmospheric turbulence compensation to name a few. A neural network based smart sensor is described that can accomplish these tasks individually or in combination, in real-time or near real-time. As a computationally intensive example, the case of optical imaging through volume turbulence is addressed. For imaging systems in the visible and near infrared part of the electromagnetic spectrum, the atmosphere is often the dominant factor in reducing the imaging system's resolution and image quality. The neural network approach described in this paper is shown to present a viable means for implementing turbulence compensation techniques for near-field and distributed turbulence scenarios. Representative high-speed neural network hardware is presented. Existing 2-D cellular neural network (CNN) hardware is capable of 3 trillion operations per second with peta-operations per second possible using current 3-D manufacturing processes. This hardware can be used for high-speed applications that require fast convolutions and de-convolutions. Existing 3-D artificial neural network technology is capable of peta-operations per second and can be used for fast array processing operations. Methods for optical imaging through distributed turbulence are discussed, simulation results are presented and computational and performance assessments are provided.

Keywords: horizontal path imaging, adaptive optics, image reconstruction, cellular neural networks, turbulence compensation, image processing

1. INTRODUCTION

Neural network techniques and methods have been successfully applied to solve a variety of complex engineering problems. Applications of interest to the defense and intelligence communities include high speed signal and image processing, image fusion, pattern recognition, target tracking, medical applications, and signal analysis[1]. Some other applications include inspection, quality control, entertainment, automotive, and security[2, 3].

A particularly difficult application is that of compensating for the effects of atmospheric turbulence in optical and near-infrared incoherent imaging systems. However, with the advent and development of fast neural network hardware and software, small, rugged, adaptive real-time or near-real time smart sensors that can perform multiple functions including atmospheric turbulence compensation are on the horizon[4]. Traditional unconventional imaging techniques such as speckle imaging or phase diversity can be used to compensate for the effects of atmospheric turbulence and can be implemented on high speed neural network processors for many real-time, or near real-time applications.

Two notable neural network computing platforms are the Cellular Neural Network Universal Machine and Super-Computer (CNN-UM & SC) invented by Leon Chua from the University of California at Berkeley during the late 1980's and the three dimensional artificial neural network (3-DANN) from Irvine Sensors. The CNN-UM & SC is an analog chip with hardwired digital logic functions—the so-called analogic configuration. The 3-DANN is a very small 3-D cube of programmable processors that can be rapidly reconfigured by adjusting the weights of the neural network.

One commercially available CNN-UM & SC configuration (Bi-I) has a 2-D 128 by 128 pixel ACE16Kv-2 Cellular Neural Network (CNN) chip integrated into a 10 K-frame per second, dual sensor system that can process up to 3 tera-OPS[5]. An operation is defined as a per pixel elementary operation such as multiplication or addition of real numbers.

Unattended Ground, Sea, and Air Sensor Technologies and Applications VIII,
edited by Edward M. Carapezza, Proc. of SPIE Vol. 6231,
62310B, (2006) · 0277-786X/06/$15 · doi: 10.1117/12.661027

One of the sensors is a 1.3 mega-pixel CMOS camera and the other has the 128 by 128, CNN chip that has pixels with a linear dimension of 5 μm. There is also an on-board digital signal processor along with associated communications and input/output circuitry. Three dimensional versions of this computing paradigm that are obtainable with current manufacturing techniques are projected at peta-OPS.

Another interesting available neural network platform is Irvine Sensor's 3-DANN that has 128 layers of 128 by 128 arrays providing a volume of neural processors that can perform elementary operations at peta-OPS. The 3-DANN is about the size of a sugar-cube and integrates with their 320 MBPS data I/O cards[6]. The 3-DANN has a digital front end, analog core, and digital output to make it attractive as a stand-alone device or as a high speed co-processor to work with the CNN in accomplishing computationally heavy applications.

Section 2 provides background on the advantages of compensating for the effects of atmospheric turbulence. Additionally, some techniques that work well for conventional near-field atmospheric turbulence compensation and also for imaging through volume turbulence are discussed. Section 3 shows our simulation results. We simulate the phase diversity technique and implement this method using a CNN simulator that is based on current 2-D CNN hardware. Section 4 provides a performance assessment of the CNN as a turbulence compensating processor. The main objective is to assess how fast various CNN architectures can perform atmospheric turbulence compensation using these unconventional imaging methods. Section 5 discusses future work and Section 6 provides a summary.

2. BACKGROUND

In this section, we first discuss the potential benefits in removing atmospheric turbulence effects from collected imagery. We do not present the linear shift-invariant (LSI) optical systems model used to describe incoherent imaging through atmospheric turbulence since it is well understood and has been previously presented along with the model and background of the CNN[4]. In this paper, the CNN is considered to be the primary processing platform and the 3-DANN is used in a supporting role for high speed array processing applications such as the 2-D Fast Fourier Transform (2-D FFT) and the 2-D Inverse Fast Fourier Transform (2-D IFFT). In actuality, the 3-DANN is capable of faster processing than currently available CNN architectures; however, 3-DANN simulation, applications development environments, and application libraries are not as readily available. We finish this section with a short discussion of speckle imaging and phase diversity methods for accomplishing the atmospheric turbulence compensation.

2.1 Atmospheric turbulence effects

For many well designed imaging systems, the atmosphere is the dominant contributor to the imaging systems loss of resolution. For example, given a circular aperture, the best achievable resolution without super-resolution techniques is established by the so-called diffraction limit,

$$\Delta x_{diff} = 1.22 \frac{\overline{\lambda}}{D} z \ , \qquad (1)$$

where $\overline{\lambda}$ is the center wavelength of the illuminating light, D is the diameter of the entrance pupil of the imaging system (e.g. diameter of the telescope, or camera lens), and z is the distance between the imaging system's entrance pupil and the object to be imaged.

This upper limit on the spatial resolution is often not achievable because of atmospheric turbulence effects. The effect of atmospheric turbulence on an incoherent imaging systems spatial resolution (ignoring system effects) is often expressed in terms of the atmospheric coherence length (a.k.a. Fried parameter), r_o, such that,

$$\Delta x_{atm} = 1.22 \frac{\overline{\lambda}}{r_0} z \ . \qquad (2)$$

The parameter r_o varies from site to site and may range from 6 *cm* to 20 *cm* for near-field turbulence conditions and 1 *cm* to 4 *cm* for imaging over horizontal paths[7]. The expected increase in resolution of an optical imaging system with diameter *D* and Fried parameter r_o is obtained by dividing equation *(2)* by equation *(1)*,

$$R = \frac{\Delta x_{atm}}{\Delta x_{diff}} = \frac{D}{r_0}. \qquad (3)$$

If the diameter of the imaging system's entrance pupil and the value of r_o is known, equation *(3)* can be used to determine the maximum achievable increase in spatial resolution assuming that the atmospheric turbulence is fully compensated and also that the system effects are negligible.

2.1 Turbulence compensation methods

Speckle imaging has been demonstrated in near field atmospheric turbulence compensation applications such as is the case for imaging airborne or astronomical objects from the ground[8]. Speckle imaging has also been used to image through volume turbulence over horizontal paths[7].

One disadvantage of the speckle imaging method is that it often requires an external reference source (such as a star) to make the method work. Notably, this is not the case for the horizontal path application of speckle imaging by Carrano[7]. The external reference was replaced by an analytical transfer function developed by Korff[9]. The Korff transfer function can be expressed as a function of the Fried parameter r_o.

Another disadvantage of the speckle imaging technique is that often many image frames (sometimes hundreds) need to be captured and processed to obtain a reasonable signal to noise ratio for qualitatively good results. Even with high speed parallel processors, this last consideration prevents the speckle imaging technique from being used in many practical real-time applications. Never-the-less, the speckle imaging method can be used for many near real-time applications[4].

Another technique that can be used for both near-field and distributed turbulence applications is the Phase Diversity (PD) method. The PD method is well understood and has been used for a variety of applications to include solar granulation studies[10], phasing multi-aperture telescopes[11], and sensing unknown aberrations in the optical path[12] to name a few. PD is known to work when imaging extended objects and is also practical when imaging through volume turbulence[13] although some improvements are expected by including amplitude effects.

As a minimum, the PD technique requires only a single pair of images—a set of in-focus and out-of-focus images that are captured at the same instant and "see" the same atmospheric turbulence. The spectra of these two images are used with parameterized estimates of the in-focus and defocused optical transfer functions to estimate the un-aberrated object brightness. An error metric, such as the one developed by Gonsalvez[14, 15], can be used to estimate the in-focus and defocused optical transfer functions. In our case we used the following Gonsalvez error metric,

$$E = \sum_{\vec{f}} \frac{\left| I\left(\vec{f}\right)\hat{H}_d\left(\vec{f}\right) - I_d\left(\vec{f}\right)\hat{H}\left(\vec{f}\right)\right|^2}{\left|\hat{H}\left(\vec{f}\right)\right|^2 + \left|\hat{H}_d\left(\vec{f}\right)\right|^2}, \qquad (4)$$

where $I\left(\vec{f}\right)$ and $I_d\left(\vec{f}\right)$ are the in-focus and defocused aberrated image spectra, $\hat{H}\left(\vec{f}\right)$ and $\hat{H}_d\left(\vec{f}\right)$ are the estimates of the in-focus and defocused optical transfer functions respectively and the sum is over all spatial frequencies in the pass-band of the OTF.

The in-focus OTF is estimated by first expanding the pupil plane phase in a convenient parameterized basis set, then forming the generalized pupil function (GPF). The in-focus OTF can then be obtained by either normalizing the autocorrelation of the GPF or by first determining the in-focus optical system's impulse response, its point spread

function (PSF), and then normalizing the spectrum of the PSF. The defocused OTF is estimated in the same fashion as the in-focus OTF except an additional known defocus term is added to the entrance pupil phase. As such, the estimate of the in-focus OTF is identical to the defocused OTF except for the known defocus phase term.

The basis set that we used are the Zernike polynomials since 1) much of the literature uses this convenient basis set, 2) atmospheric aberrations can be decomposed into well understood and practical components such as piston, tilt, astigmatism, coma, etc., and 3) our turbulence generating simulator lets us add controllable amounts of these turbulence components.

The generalized pupil plane phase is estimated from the following weighted sum of Zernike polynomials[8],

$$\phi(R\rho,\theta)=\sum_{i=1}^{n} a_i Z_i(\rho,\theta), \tag{5}$$

where a_i are the weights on the i^{th} Zernike polynomial $Z_i(\rho,\theta)$ and ρ and θ are pupil plane coordinates expressed as a normalized pupil plane radius $\left(\rho=\sqrt{x^2+y^2}\Big/R\right)$ where x and y are the components of the entrance pupil plane coordinate $\vec{x}$, R is the radius of the circular entrance pupil, and θ is the angular component of $\vec{x}$. The Zernike functions themselves are listed according to Noll's ordering scheme[16].

Estimates of the OTFs are made by first determining the weights on the Zernike, polynomials, forming the generalized pupil function phase, and then calculating the PD OTFs as a function of the Zernike weights. Optimization techniques or iterative search methods can be employed to efficiently determine the Zernike weights by minimizing the error metric shown in equation *(4)*. The result is an estimate of the PD OTFs $\hat{H}(\vec{f})$ and $\hat{H}_d(\vec{f})$. The inverse of $\hat{H}(\vec{f})$ can be used to determine the compensating filter function[4]. A "corrective" PSF can be found by a 2-D inverse Fast Fourier Transform (IFFT) of the compensating filter function.

The turbulence compensated image can be obtained either by using the CNN to de-convolve the atmospheric turbulence effects directly using the corrective Point Spread Function, or by using the CNN or Irvine Sensor 3-DANN to inverse 2-D Fourier Transform the product of the turbulence degraded image spectrum with the compensating filter function. The later approach is generally much faster but may not be in the future with evolving CNN hardware.

Note that the single entrance pupil plane phase screen model under isoplanatic imaging conditions of the OTFs in the near-field LSI turbulence model is strictly speaking not accurate for horizontal path imaging conditions. However, previous results have shown that, for mild turbulence, there is a certain resilience to this type of error and mosaic processing methods may be used [13, 17]. For stronger turbulence, a distributed phase screen model was shown to be effective with further improvements expected by including amplitude effects. To establish a baseline for our work, we start with a mild horizontal path turbulence assumption so that our image can be broken into smaller regions where isoplantic, LSI imaging models are valid. In subsequent work, we plan to investigate distributed phase screen models and also include amplitude effects.

3. RESULTS

In this section, we present our simulated results. We use a turbulence generating simulator to generate aberrated in-focus and defocused images from a reference image with controllable amounts of atmospheric turbulence. These aberrated images are used in a phase diversity simulator to estimate the in-focus and defocused entrance pupil phases and subsequently the in-focus and defocused OTFs. The estimated in-focus OTF is used to generate a compensating filter function and subsequently a corrective Point Spread Function. A CNN simulator based on current 2-D hardware capabilities is used to remove the turbulence.

In Figure 1, we have used the atmospheric turbulence simulator to generate some common Zernike aberrations. The left figure shows the entrance pupil phase map generated with an *x*-tilt and *y*-tilt each with a weight of 2 radians. As expected, the resulting phase is a plane with a positive slope in both the *x* and *y* directions. The *x*-axis is shown originating from zero and running to the right to 150. The *y*-axis of Figure 1 runs from center to left (0 to 150).

Figure 1: Zernike polynomial generated entrance pupil phases. The left figure shows the phase of an x-tilt and y-tilt with amplitude of 2 radians. The right figure shows the Zernike polynomial generated phase for the defocus term weighted with amplitude of 2 radians.

The plot on the right side of Figure 1 is the entrance pupil plane phase obtained from only the defocus Zernike polynomial with amplitude of 2 radians. According to the Noll ordering scheme, this would be $Z_4(R\rho,\theta)$. Our turbulence simulator can generate up to 36 Zernike modes allowing us to "dial-in" individually controllable amounts of atmospheric turbulence.

Figure 2 shows our reference image on the left and a blurred image using the first 6 Zernike polynomials. The first 3 Zernike coefficients were set to zero since these do not affect the image quality.

Figure 2: Left is the un-aberrated reference object brightness. Right is the aberrated image generated using the 4th through 6th Zernike polynomials all weighted by 2 radians.

The first Zernike term (piston) makes no difference in single aperture telescope systems and the second (*x*-tilt) and third (*y*-tilt) just move the image around the focal plane. The weights on the 4th through 6th Zernike terms were set to 2 radians. Figure 3 shows the Optical Transfer Functions due to these Zernike aberrations for both the in-focus and defocused images.

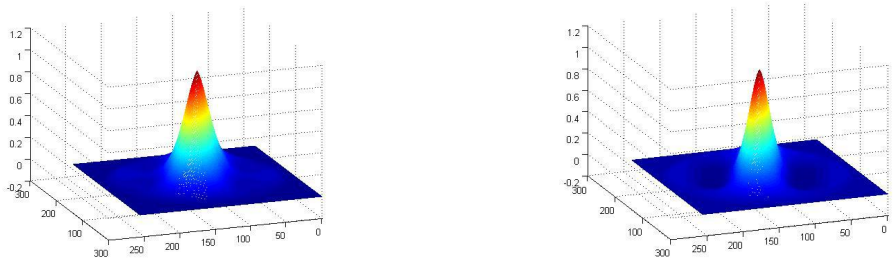

Figure 3: Left is a plot of the real part of the optical transfer function associated with Zernike modes 4 through 6. This OTF was used to blur the reference image. The OTF on the right is associated with the defocused image.

The left figure shows the real part of the OTF and contains effects due to the aperture and also the 4th through 6th dialed in Zernike terms as well. The OTF associated with the left image was used to filter the spectrum of the reference image to effectively "blur" the image with the proscribed amounts of atmospheric turbulence. The OTF associated with the right image of Figure 2 was used to generate the defocused image. The second OTF in Figure 3 contains the same aberrations as the one on the left but has an additional prior known defocus term (unit amplitude quadratic phase in this case).

Figure 4: The figure on the left is the in-focus blurry image aberrated with Zernike coefficients 4 through 6. The right figure is the blurry image aberrated with Zernike coefficients 4 through 6 with an additional unit amplitude defocus term.

Figure 4 shows the resulting images in applying the OTFs illustrated in Figure 3. The figure on the left is the reference image blurred with the aberrating OTF shown on the left of Figure 3 and the image on the right is the reference image blurred with the defocused aberrating OTF shown on the right of Figure 3. You can see that the image due to the defocused aberrating OTF is slightly worse in a qualitative sense than the image from the aberrated OTF and that both images in Figure 4 are worse than the reference image.

The PD method was applied to the blurry images shown in Figure 4. The inputs to the algorithm are the in-focus and defocused blurry images shown in Figure 4. The PD technique estimates the Zernike coefficients for each of the Zernike modes, reconstructs the entrance pupil plane phase, and then estimates the in-focus and defocused aberrating OTFs. Figure 5 shows the reconstructed aberrating OTFs obtained from the PD method.

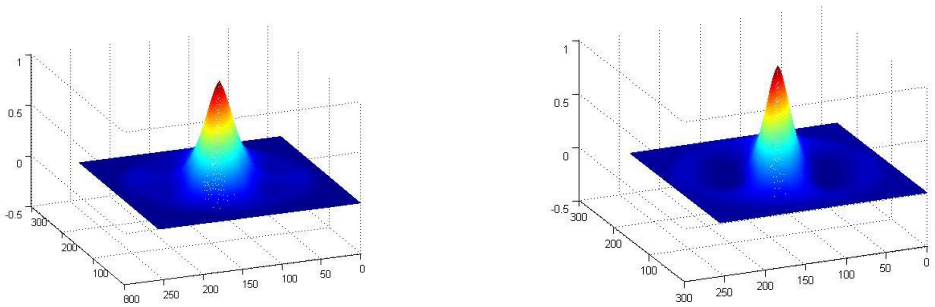

Figure 5: Phase Diversity estimates of the in-focus and defocused aberrating OTFs. The left figure is the phase diversity estimate of the OTF shown on the left of Figure 3. The right figure is the phase diversity estimate of the OTF shown on the right of Figure 3.

Good agreement is seen between the PD reconstructed OTFs and the reference OTFs shown in Figure 3.

The CNN simulator was used to "correct" the turbulence degraded image. A corrective point spread function based on the inverse of the estimated OTF obtained from the phase diversity method was used to remove the atmospheric turbulence effects. Figure 6 shows both the aberrated image using the 4th through 6th Zernike polynomial (left) and the simulated CNN corrected image (right).

Figure 6: The left figure shows the aberrated image using the 4th through 6th Zernike polymials. The right figure is the "corrected" figure using the phase diversity technique implemented with the CNN simulator.

The PD and CNN corrected image is much better than the aberrated image and recovers much of the spatial information present in the original reference image.

4. PERFORMANCE ASSESSMENT

This section discusses the computational issues associated with implementing the unconventional imaging methods such as the phase diversity technique on the CNN. The approach taken is to break down the phase diversity method into a finite set of high level operations such as point-wise transcendental functions such as square root, square, trigonometric, logarithmic, and exponential functions.

These higher level functions can be implemented by the COordinate Rotation DIgital Computer (CORDIC) system which has the convenient characteristic that the same set of three iterative equations with different weights can be used to compute any of these functions. Further, the desired accuracy is just a function of the number of iterations of these governing equations along with sufficient computer memory. Finally, the three governing CORDIC equations consist only of elementary operations of add, subtract or multiplication of real numbers. These elementary operations can be implemented on the CNN and on the 3-DANN.

The estimated time required in executing a particular high level operation is just the total number of elementary computations it takes to implement the higher level function divided by the processor's speed in elementary operations per second. It should be noted that series expansions can sometimes be used for faster convergence of some of the functions and that these would then be used where necessary. In our timing studies, we used the CORDIC system due to the selectable accuracy being a function of the number of iterations of the governing CORDIC equations and that the majority of the required functions for the phase diversity technique could be implemented using the CORDIC system. Additionally, for a given accuracy, a wide variety of high level functions would have the same number of elementary operations. The CORDIC system can also be used to implement the Discrete Fourier Transform.

With regards to processing speed, current 2-D versions of the CNN are capable of 3 tera-OPS in analog mode and are projected at peta-OPS in 3-D analog mode. Irvine Sensor's 3-DANN currently can operate at peta-OPS. These quoted high speeds are due to the fact that the number of pixels in the processor provides an effective processing gain. For instance, for a 128 by 128 2-D CNN array, the 3 tera-OPS means that a single pixel is actually processing at approximately 183.105 mega-OPS ($3 \times 10^{12}/128^2$). The entire 128 by 128 array of pixels is processed in parallel during one cell iteration and settle time. Each pixel can be independently processed and so the effective number of elementary computations is 3 tera-OPS.

Table 1 shows the estimated processing time on a per pixel basis for higher level functions that are fundamental to the phase diversity and other unconventional imaging methods. The 2-D convolution, 2-D FFT, and 2-D IFFT were determined previously[4]. The numbers shown for the 2-D convolution assume a 256 by 256 input image with a 256 by 256 point spread function. The digital emulation mode numbers are not shown for the 2-D convolution because current hardware is not optimal for these types of computations—current digital emulation hardware comes in a 40 pixel wide linear array[18] and the processing time is not practical for our high-speed 2-D convolutions for our unconventional imaging applications.

Elementary Mode	Operations (real)	Digital Emulation mode	2-D CNN Analog Mode	3-DANN/3-D CNN
Complex Addition	2 parallel	*1 ns*	*0.333 ps*	*1 fs*
Complex Subtraction	2 parallel	*1 ns*	*0.333 ps*	*1 fs*
Complex Multiplication	4 parallel 2 parallel	*2 ns*	*0.667 ps*	*2 fs*
Complex Conjugation	2 parallel	*1 ns*	*0.333 ps*	*1 fs*
Division	single	*0.496 μs*	*0.165 ns*	*0.496 ps*
2-D FFT	single	*0.2785 ms*	*92.843 ns*	*0.2785 ns*
2-D IFFT	single	*0.3441 ms*	*114.668 ns*	*0.3441 ns*
2-D Convolution (256 x 256)	single	*n/a*	*11.409 ms*	*34.423 μs*
Elementary Operations	single	*1 ns*	*0.333 ps*	*1 fs*
CORDIC Functions	single	*0.72 μs*	*0.24 ns*	*0.72 ps*

Table 1: Per cell computation estimate for higher level functions necessary for unconventional imaging applications.

For the CORDIC functions, forty seven iterations are assumed providing accuracy out to 16 digits. For the division operation, a slow subtraction algorithm was assumed with accuracy out to 16 digits. In using Table 1, care must be taken when making timing estimates since some serial operations must wait for the entire array (2-D) or volume (3-D) to be processed before proceeding to the next calculation. Also, memory access and on-board data I/O are negligible when complex tasks are undertaken[1]. For this reason, we assume on board memory/data I/O are part of the quoted OPS of the processors.

Another way of looking at the timing is to consider the time constant of the CNN itself. These have been quoted at 200 *ns* for actual CNN hardware[1]. Dependent on the application (convolution, erosion, etc.), the cell iteration time—the time it takes the CNN to perform the complex operation—can be specified in terms of number of CNN time constants. For instance, it takes 6 CNN time-constants τ_{CNN} to perform a 128 by 128 convolution with a 3 by 3 kernel[1]. Since the CNN time-constant depends on the physical factors of the hardware itself (such as pixel dimensions, material type, and resistance and capacitance of the material, we will use the more generic OPS analysis to investigate the timing.

Processing estimates were made for the phase diversity technique using the quoted 3-D OPS of the CNN architecture and the 3-DANN. Initial image acquisition was determined based on using an image acquisition system of 320 MBPS. This is well within the capability of conventional frame grabber cards. The phase diversity technique was broken into two parts, an image acquisition sequence and a phase diversity processing sequence. Each sequence was broken into a series of functional steps using the higher order functions outlined in Table 1. For each functional step, a decision was made on whether-or-not the entire array needed to be computed before executing the next functional step. If so, then the array processing time was used in the timing estimates instead of the single cell timing estimates shown in Table 1. For comparison, the process was repeated for the speckle imaging technique. The parallel nature of the CNN and 3-DANN architecture was applied where applicable. Table 2 shows the results of the timing study.

Unconventional Imaging Method	Acquisition Time (sec)	Processing Time (sec)	Total time (sec)
Phase Diversity	*52.423 ms*	*49.781 ms*	*0.1022 s*
Speckle Imaging	*10.486 s*	*48.808 ms*	*10.535 s*

Table 2: Estimated processing time for unconventional imaging methods on various CNN architectures.

In performing the timing study, many opportunities exist for optimizing the calculations and further reducing the required number of computations and the corresponding total processing time. For instance, in the phase diversity technique time estimate, more sophisticated optimization techniques, the use of series expansions for some of the CORDIC transcendental functions, the use of symmetry relationships and table look-ups in the computation of the 2-D FFT/IFFT, and fast division methods will reduce the total processing time estimated even further than the times given in Table 2. Also, parallel computation of the Zernike weights can further reduce the phase diversity processing timing estimate to approximately *1.383 ms*.

In addition to the processing time, other important considerations that factor into a technology employment decision are power, size, and the dynamic range of the processor. A recent 2-D analog implementation of the CNN has 3 orders of magnitude superiority in speed, area, or power over equivalent digital representations[1]. A CNN based smart-pixel architecture with hardware annealing capability and programmable digital synaptic weights was presented by a Jet Propulsion Laboratory, University of Southern California, and German Aerospace Research Establishment team for space-based smart sensing applications[19]. The proposed Intelligent Multi-sensor System (IMS) has a hybrid CNN-based processing system that requires 7 watts (as opposed to 1475 watts for traditional systems). This system also uses a vertical CMOS-BJT as a photo-transistor integrated with a pair of transistors in a Darlington configuration that provide 20 μA of current with a dynamic range of 100 dB[20]. Walkman size devices that are capable of processing peta-OPS on 200 by 200 arrays are possible.

5. FUTURE WORK

We plan on looking at system engineering aspects in developing a rugged, portable, turbulence compensation system based on the CNN paradigm. We also want to implement the phase diversity method on the Bi-I cellular neural network system as an operational proto-type sensor for both near-field and horizontal path imaging scenarios. The experimental results can then be compared to our simulated results. Investigating alternate 2-D and 3-D neural systems implementation approaches and architectures are also planned.

6. SUMMARY

This paper looked at the benefits of removing atmospheric turbulence from imagery collected with passive, incoherent imaging sensors. The size of the imaging systems entrance pupil when compared to the Fried parameter r_o indicates the relative improvement in spatial resolution that can be expected by compensating for the atmospheric turbulence effects. A short discussion on when an optical imaging system would benefit from atmospheric turbulence compensation was presented. For linear shift-invariant systems, the CNN paradigm can be used as either an optical systems simulator or for an atmospheric turbulence compensation processor. The phase diversity method was presented as a viable technique for both near-field and distributed turbulence compensation. We simulated controllable amounts of atmospheric turbulence and showed how the phase diversity method could remove the turbulence given only an in-focus and defocused aberrated pair of images. A CNN simulation based on current available 2-D hardware processing capabilities was then performed to implement the phase diversity technique. A performance assessment was done to determine how fast the phase diversity method could be implemented on the CNN architecture and this was compared to another unconventional imaging method used for both near-field and distributed atmospheric turbulence compensation—speckle

imaging. Using processing estimates from a 3-D analog CNN architecture, the phase diversity method was shown to be suitable for real-time implementations whereas the speckle imaging technique is appropriate for many near real-time applications.

ACKNOWLEDGEMENTS

We would like to thank the National Center for Hydrogen Research at Florida Institute of Technology and DIA/DTT-1 for conference support. I also want to thank my students, especially Rachael Singer with her help with the phase diversity simulator.

REFERENCES

1. Leon O. Chua, and Tamas Roska, *Cellular neural networks and visual computing foundations and applications*, Cambridge University Press (2002).
2. Frederic M.Ham, and Ivica Kostanic, *Principals of Neurocomputing for Science and Engineering*, McGraw Hill (2001).
3. T. Roska, and J. Vandewalle, *Cellular Neural Networks*, Wiley, 1993.
4. W. W. Arrasmith, "High Speed Atmospheric Turbulence Compensation using a Cellular Neural Network", Military Sensing Symposium: Passive Sensors, Orlando, FL, February 13, 2006.
5. Bi-I Specification sheet, obtained from Anafocus homepage at, http://www.eutecus.com, (cited February, 2006).
6. 3-DANN Specifications sheet, obtained from Irvine Sensors homepage at, http://www.irvine-sensors.com, (cited February, 2006).
7. C. J. Carrano, "Speckle Imaging over horizontal paths", SPIE Conference on Wavefront Control, Seattle, WA, July 8, 2002.
8. Michael C. Roggemann, and Byron Welsh, *Imaging through Turbulence*, CRC Press (1996).
9. D. Korff, "Analysis of a method for obtaining near-diffraction-limited information in the presence of atmospheric turbulence", J. Opt. Soc. Am., Vol. 63, No. 8, pp. 971- 980, 1973.
10. J. H. Seldin and R. G. Paxman, "Phase-Diverse Speckle Reconstruction of Solar Data," In *Image Reconstruction and Restoration*, T. J. schulz and D. L. Snyder, eds., Proc. SPIE **2302**, 268-280 (San Diego, CA 1994).
11. R. G. Paxman and J. R. Fienup, "Optical misalignment sensing and image reconstruction using phse diversity," J. Opt. Soc. Am. A, Vol. 5, No. 6, pp. 914 – 923, 1988.
12. D. J. Lee, Byron M. Welsh, M. C. Roggemann, and B. L. Ellerbroek, "Diagnosing unknown aberrations in an adaptive optics system by use of phase diversity," Optics Letters, Vol. 22, No. 13, pp. 952 – 954, 1997.
13. B. J. Thelen, , D. A. Carraras, , and R. G. Paxman, "Fine-resolution imagery of extended objects observed through volume turbulence using phase-diverse speckle", SPIE Conference on Propagation and Imaging through the Atmosphere, Denver, CO, July 1999.
14. R. A. Gonsalves, "Phase Retrieval from Modulus Data," J. Opt. Soc. Am., Vol. 66, No. 9, September 1976.
15. R. A. Gonsalves and R. Chidlaw, "Wavefront Sensing by Phase Retrieval," SPIE. Vol. 207, Applications of Dgital Image Processing III, 1979.
16. R. J. Noll, , "Zernike Polynomials and atmospheric turbulence," *J. Opt. Soc. Am.*, Vol. 66, pp. 207-211, 1976.
17. R. G. Paxman, B. J. thelen, and J. H. Seldin, "Phase-diversity correction of turbulence-induced space-variant blur," Optics Letters, Vol. 19, No. 16, pp. 1231 – 1233, 1994.
18. T. Hidvegi, I. Suto, P. Keresztes, and P. Szolgay, "Interfacing the CASTLE emulated digital array processor to the ALADDIN system", European Conference on Circuit Theory and Design, Krakow, Poland, 31 August, 2003.
19. W. Fang, B. J. Sheu, H. Venus, and R. Sandau, "Smart-Pixel Array Processors based on Optimal Cellular Neural Networks for Space Sensor Applications," IEEE Proceedings of the International Conference on Computer Design: VLSI in computers and processors, Austin, TX, October 2 – 4, 1995.
20. C. A. Mead, *Analog VLSI and Neural Systems*, Addison-Wesley Publishing Company, MA (1989).